High-resolution and super stacking of time-reversal mirrors in locating seismic sources

W. Cao[1], S. M. Hanafy[2*], G. T. Schuster[2], G. Zhan[2] and C. Boonyasiriwat[2]

[1]*Chevron Energy Technology Company, 1500 Louisiana St, Houston, TX 77002, USA, and* [2]*King Abdullah University of Science and Technology, Mail box 1547, Thuwal 23955-6900, Saudi Arabia*

ABSTRACT

Time reversal mirrors can be used to backpropagate and refocus incident wavefields to their actual source location, with the subsequent benefits of imaging with high-resolution and super-stacking properties. These benefits of time reversal mirrors have been previously verified with computer simulations and laboratory experiments but not with exploration-scale seismic data. We now demonstrate the high-resolution and the super-stacking properties in locating seismic sources with field seismic data that include multiple scattering. Tests on both synthetic data and field data show that a time reversal mirror has the potential to exceed the Rayleigh resolution limit by factors of 4 or more. Results also show that a time reversal mirror has a significant resilience to strong Gaussian noise and that accurate imaging of source locations from passive seismic data can be accomplished with traces having signal-to-noise ratios as low as 0.001. Synthetic tests also demonstrate that time reversal mirrors can sometimes enhance the signal by a factor proportional to the square root of the product of the number of traces, denoted as N and the number of events in the traces. This enhancement property is denoted as super-stacking and greatly exceeds the classical signal-to-noise enhancement factor of $\sqrt{N}$. High-resolution and super-stacking are properties also enjoyed by seismic interferometry and reverse-time migration with the exact velocity model.

Key words: Mining, Passive method, Time reversal mirrors.

INTRODUCTION

Accurately locating seismic sources is a fundamental problem in seismology. To locate earthquakes, arrival times are picked for events in recorded seismograms and seismic sources are located by minimizing the difference between the observed and predicted arrival times (Thurber and Rabinowitz 2000), or using the arrival time differences between events (Waldhauser and Ellsworth 2000). For these schemes, the signal-to-noise (S/N) ratio of the recorded data needs to be high enough to facilitate the picking of arrival times. To avoid picking arrival

times, McMechan (1982), Gajewski and Tessmer (2005) and McMechan, Luetgert and Mooney (1983) used a reverse-time modelling technique in which the recorded seismic data are used as time histories of virtual sources at the geophones, and the resulting wavefields are numerically backpropagated to the source location. In this scheme arrival times do not need to be picked from the seismograms and ideally, all events can be focused at the source location with maximum amplitude. This is similar to the time reversal mirrors method (Fink 1993, 1997, 2006), where recorded wavefields from a source are physically backpropagated in the medium and focused at the source location at zero time. With the correct velocity model, the reverse-time modelling scheme can be viewed as the numerical version of the time reversal mirror method.

*E-mail: sherif.geo@gmail.com

In this paper, we propose to locate seismic sources by applying the time reversal mirror method to recorded seismic data. Assuming that we have recorded the band-limited natural Green's functions[1] for the pre-recorded source locations and the actual receiver locations, we correlate these trial band-limited Green's functions with the recorded data and the trial band-limited Green's function so that the maximum correlation value indicates the actual source location. Here the procedure for backpropagating the recorded data is replaced by correlating data traces with the Green's function traces. For this scheme, the source can be located without knowledge of the velocity model. The application presented in this paper is for locating miners trapped in collapsed mines and is implemented in two steps:

1 We first record the band-limited natural Green's functions for different source positions in the mining tunnel and the surface receivers before the mine collapses.

2 In the case of a mine collapse, the seismic signals are generated by the miner's hammer striking the side of the mining tunnel and are recorded by the surface receivers; correlating these recorded traces with the pre-recorded band-limited Green's functions gives the miner's location. We also apply a trial time shift to the location process to compensate for the unknown source-excitation time.

In our approach, where the recorded band-limited Green's functions are used to focus the passive signal to the source location, both high-resolution and super-stacking can be utilized to enhance the identification of the source location. High-resolution of the time reversal mirror method is originally demonstrated in experiments with multiple scattering (Derode, Roux and Fink 1995; Roux and Fink 2000; Fink 2006) showing much higher spatial resolution than the Rayleigh resolution limit. Part of the enhanced resolution is due to multiple scattering events that partially widen the effective recording aperture.

This paper is organized in the following way. The theory of time reversal mirror will be first introduced, followed by a discussion of its high-resolution and super-stacking properties. These properties are demonstrated using synthetic data for locating trapped miners in collapsed mines. The final part shows tests with field data acquired along a cliff in Moab, Utah.

---

[1]In this paper the natural Green's function or simply the Green's function refers to a band-limited Green's function due to a point source modified by the source wavelet.

THEORY

Imaging the location of seismic sources is similar in methodology to estimating the subsurface reflectivity distribution by poststack migration, except that only one-way propagation is considered for the source imaging. For passive seismic data with unknown source excitation times, a trial time shift is applied to the traces to compensate for the unknown excitation times. The migration amplitudes are compared for different time shifts and the localized maximum of migration amplitudes pinpoints the unknown source locations. This imaging condition is similar to that used for reverse time migration (Gajewski and Tessmer 2005) except with time reversal mirrors no velocity model is needed.

Imaging seismic sources can be formulated using the approximate equation for poststack migration:

$$m(\mathbf{x}) = \sum_{\mathbf{g}} [d(\mathbf{g}, t|\mathbf{s}, 0) \otimes g(\mathbf{g}, t|\mathbf{x}, 0)]|_{t=0}, \tag{1}$$

where $d(\mathbf{g}, t|\mathbf{s}, 0)$ denotes the second time derivative of the seismic data recorded at $\mathbf{g}$ with the source excited at time 0, $g(\mathbf{g}, t|\mathbf{x}, 0)$ is the Green's function for a source at $\mathbf{x}$ excited at time 0 and the receiver at $\mathbf{g}$, $\mathbf{x}$ is the trial image point and $\otimes$ denotes the temporal correlation operator. For a conventional Kirchhoff type migration, the Green's function $g(\mathbf{g}, t|\mathbf{x}, 0)$ is sometimes approximated by $\delta(t - \tau_{gx})$, where τ_{gx} is the direct-wave traveltime between $\mathbf{x}$ and $\mathbf{g}$ computed by ray tracing in an assumed velocity model. Then equation (1) can be simplified as:

$$m(\mathbf{x}) = \sum_{\mathbf{g}} d(\mathbf{g}, \tau_{\mathbf{gx}}|\mathbf{s}, 0). \tag{2}$$

Usually the source excitation time is unknown and a trial time shift t is introduced into the equation to compensate for the unknown source excitation time,

$$m(\mathbf{x}, t) = \sum_{\mathbf{g}} d(\mathbf{g}, \tau_{gx} + t|\mathbf{s}, t_{source}), \tag{3}$$

where $d(\mathbf{g}, \tau|\mathbf{s}, t_{source})$ represents the differentiated seismic data recorded at time τ and location $\mathbf{g}$ for a source at $\mathbf{s}$ with unknown excitation time t_{source}. Choosing the trial excitation time $t \to t_{source}$ and trial source location $\mathbf{x} \to \mathbf{s}$ yields the maximum migration amplitude at $\mathbf{s}$.

A problem with this approach is that passive data are often very noisy with a limited recording aperture so that a migration amplitude does not contain an unambiguous maximum, leading to poor resolution of the source location. Another major problem is that a velocity model is needed to compute the traveltime τ_{gx} by ray tracing. However, if the natural Green's

functions are recorded for sources at imaging points and receivers on the surface, we can migrate the data with the natural Green's functions (Schuster 2002), i.e.,

$$m(\mathbf{x}, t) = \sum_g d(\mathbf{g}, t|\mathbf{s}, t_{source}) \otimes [w(t) * g(\mathbf{g}, t|\mathbf{x}, 0)], \qquad (4)$$

where $[w(t) * g(\mathbf{g}, t|\mathbf{x}, 0)]$ represents the pre-recorded data for a point source at $\mathbf{x}$ and geophone at $\mathbf{g}$. Here, $w(t)$ is the band-limited source wavelet and $g(\mathbf{g}, t|\mathbf{x}, 0)$ is the impulse response of the medium. The natural Green's function accounts for the direct wave but also contains all of the primaries, diffractions and multiples. These multiple-scattering events can be utilized for imaging with the properties of both high-resolution (Derode *et al.* 1995; Roux and Fink 2000; Fink 2006) and super-stacking (see Fig. 1). Moreover, if scatterers are within one wavelength of the source, then evanescent energy can be converted to propagating waves and greatly increase the resolution of the image (Vigoureux, Depasse and Girard 1992; Fink 2008; Zhang and Liu 2008). Finally, a velocity model is not needed because $g(\mathbf{g}, t|\mathbf{x}, 0)$ is recorded rather than computed.

Figure 1 illustrates the super-stacking feature of time reversal mirrors where a buried source excites the scattered events seen in (a). Here, a buried source at $t = 0$ excites direct waves, primary reflections, and multiples that are recorded along the surface. Backpropagating this wavefield using equation (4) is equivalent to replacing the geophones by point sources, time reversing the traces and using them as the respective source time-history functions. As suggested in Fig. 1(b), backward modelling coherently returns the recorded events to their common source position at the excitation time of $t = 0$. This

means that the estimated migration amplitude is maximum at the source point $\mathbf{s}$ at $t = 0$ because all of the backprojected direct waves, primaries and multiples are simultaneously in phase at the source excitation time ($t = 0$ in this example). The multiple scattered arrivals typically have a wider range of ray angles with respect to the source position and so provide a higher resolution image of the source compared to imaging only with direct arrivals.

This imaging procedure is, for a trial image point at $\mathbf{s}$, approximately equivalent to summing the direct wave amplitudes along the solid hyperbola in Fig. 1(b), as well as summing along the dashed hyperbolas associated with the primaries and multiples (Schuster 2002). In contrast, the standard migration described by equation (3) only sums along the direct wave hyperbola. For additive uncorrelated white noise, the standard migration enhances the signal-to-noise (S/N) ratio in the migration amplitude by a factor of $\sqrt{N}$ (see Appendix A), where N is the number of traces in the data $d(\mathbf{g}, \tau|\mathbf{s}, t_{source})$. Instead of just summing along the direct wave hyperbola, the time reversal mirror approach in equation (4) coherently sums all of the events in the records into the migration amplitude. Compared to the standard migration, the extra term of M, which denotes the number of events in the records, enhances the signal-to-noise ratio in the time reversal mirror image by factor $\sqrt{MN}$. The detailed derivation of the enhancement factor is provided in Appendix A, where we assume that all the events have similar amplitudes. When geometrical spreading effects need to be considered, M can be replaced by a factor that roughly accounts for geometrical spreading. For example, M can be approximated by the factor $(cP + cT_1) \sum_{k=1}^{M} 1/(cPk + cT_1) =$

Figure 1 a) Forward modelled and b) time-reversed traces at the surface act as source wavelets for the virtual sources at the surface. The energy from these virtual sources focuses at the position **s** at time zero.
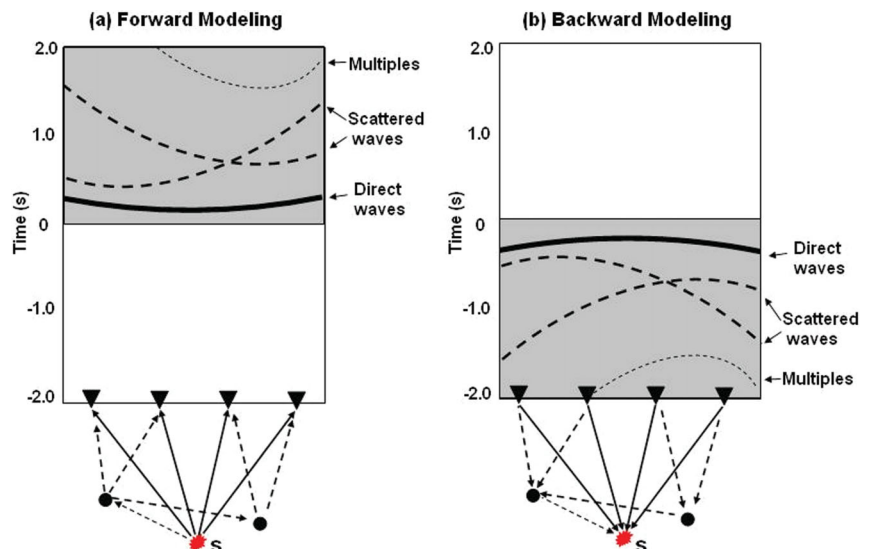
$(P + T_1) \sum_{k=1}^{M} 1/(Pk + T_1)$ where c is the average velocity, T_1 is the initial onset time of the first arrival, P is the dominant period and the kth event arrives at the time $Pk + T_1$. Here the geometrical spreading distance is approximated by $c(Pk + T_1)$.

NUMERICAL TESTS

Locating trapped miners with natural Green's function

The migration strategy associated with equation (4) is now used for the example of locating a trapped miner in a collapsed mine. Prior to the mine collapse, a permanent geophone array is deployed over the mining tunnel on the surface and communication stations that consist of a small iron plate and a hammer are set up at selected locations in the mining tunnel. Then calibration Green's functions $g(\mathbf{g}, t|\mathbf{x}, 0)$ are recorded by the surface array by using a hammer to pound the tunnel walls at the communication stations; to insure a high signal-to-noise ratio, the hammer excitation is repeated many times and the responses are stacked together. After the mine collapses, a trapped miner will find the nearest communication station and call for help by hammering at the communication stations to generate the bandlimited data $d(\mathbf{g}, t|\mathbf{s}, t_{source})$ recorded by the same array of geophones on the surface. We denote the seismic data associated with the trapped miner's signal as save our souls (SOS) calls. These data are very noisy so traditional imaging methods will not work well compared to using the time reversal mirror equation (4), as will be seen in the following example.

A finite-difference solution to the 2D acoustic wave equation is used to generate synthetic seismograms for the model in Fig. 2. Shot gathers are generated by individual sources at 201 communication stations located at $\mathbf{x}'$ along the mine tunnel and the seismograms are recorded along the earth's free surface at $\mathbf{x}$ to give a bandlimited estimate of $g(\mathbf{x}, t|\mathbf{x}', 0)$. For this test, these same seismograms are used to construct the miner's SOS call $d(\mathbf{x}, t|\mathbf{s}, 0)$, except random noise is added to these data. Clean and noisy shot gathers are shown in Fig. 3(a,b).

Equation (4) is then used to compute the migration amplitude along different parts of the mining tunnel. The results in Fig. 4(a,b) show a very good resolution of the miner's location (delineated by the large peak); in this case the signal-to-noise ratio is 1/1611. These results demonstrate the robustness of this method in the presence of strong white noise.

We also test the case when the source of the SOS call is located between two communication stations. Here we take the shot with the source at $x = 1220$ m in the mine as the SOS
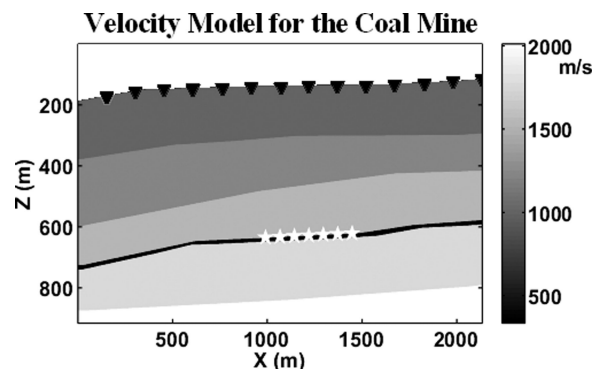

Figure 2 Velocity model containing a mine tunnel (the thick black line in the model) with a height of about 10 m located at a depth of about 670 m; 201 shot gathers were generated with 351 receivers (triangles) at the surface. Shots (stars) are evenly distributed in the tunnel from x = 915 m to x = 1525 m; the shot spacing in the tunnel is 3 m and the receiver spacing is 6 m.

call and we subsample our shooting stations by considering only every other shot. Then the source location of this SOS call is located between two communication stations. We migrate the SOS call with this half-set of Green's functions and the results are shown in Fig. 5. Though the maximum value in Fig. 5(b) does not give the actual source location, the strong peak still identifies the two communication stations closest to the source location. In this test the spacing between the two communication stations is 12 m, about 1/3 of the dominant wavelength of 38 m[2].

A potential problem with this technique is the effect of the medium change caused by the mine collapse near the active communication station, since in this case the pre-recorded Green's functions are valid for the pre-collapse mine environment while the SOS call is for the post-collapse environment. The change is referred to as the stability of time reversal mirrors with respect to changes in the medium (Scales and Snieder 1997; Snieder and Scales 1998). To investigate this issue, additional numerical tests are conducted and included in Appendix B. These tests suggest that the location of the trapped miner can sometimes be correctly identified when the medium change is up to 4 dominant wavelengths in size.

Validation of high-resolution

Synthetic data are used to validate the concept of high-resolution with time reversal mirrors. Finite-difference simu-

---

[2]The dominant wavelength is calculated by dividing the velocity at the source location by the dominant source frequency.

(a) Noise–free Shot Gather
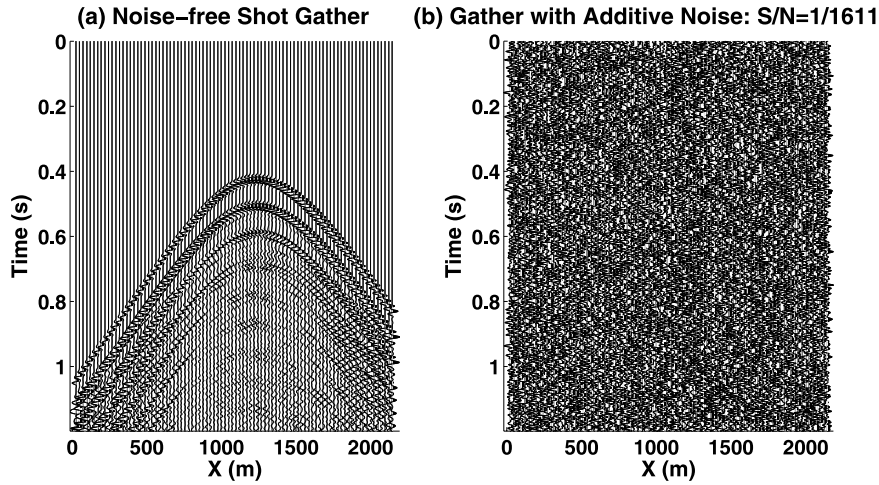
(b) Gather with Additive Noise: S/N=1/1611

Figure 3 a) Noise-free and b) noisy shot gather for a source in the mine and receivers on the surface. The signal-to-noise ratio is 1/1611 for the noisy shot gather.
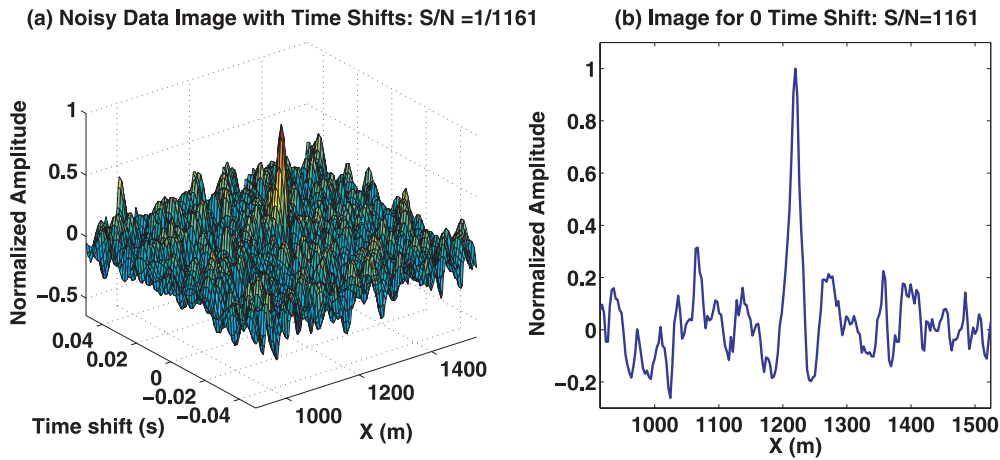
(a) Noisy Data Image with Time Shifts: S/N =1/1161

(b) Image for 0 Time Shift: S/N=1161

Figure 4 a) Migration amplitude $m(\mathbf{x}, t)$ calculated from the noisy data shown in Fig. 3(b). b) The zero time shift section $m(\mathbf{x}, 0)$ from the image shown in (a). Here the peak in the migration amplitude shows that the correct time shift is 0 and the miner is at $X = 1.219$ km.

Figure 5 Migration results when the source of the SOS is located between 2 communication stations. a) The location result with a trial time shift. The peak value occurs at the 0 time shift and the correct source location. b) The 0 time shift section of panel (a). The vertical line indicates the actual location of the source.
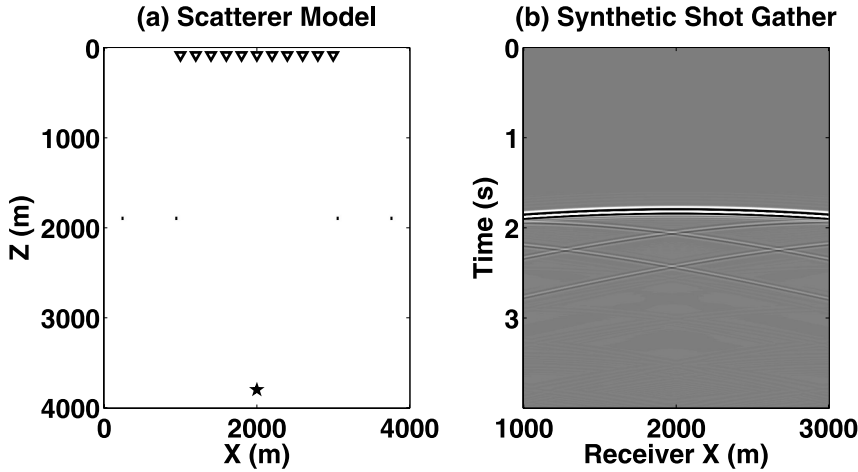
(a) Source between Communication Stations

(b) Location Result: 0 Time Shift

(a) Scatterer Model

(b) Synthetic Shot Gather
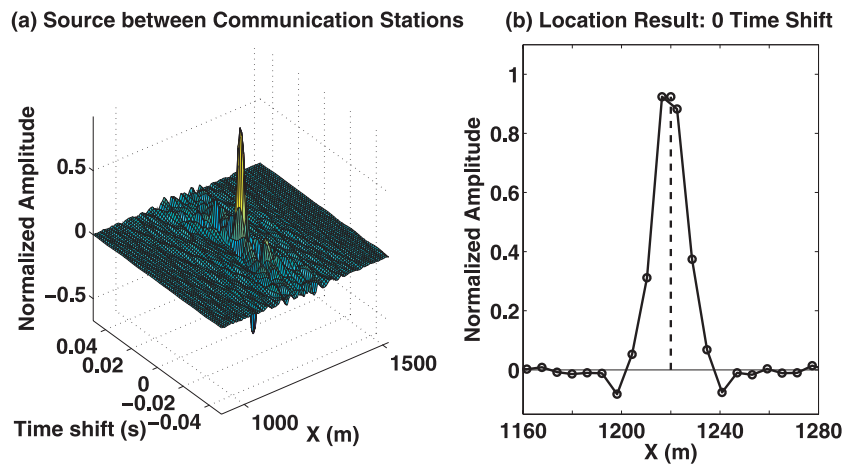
Figure 6 a) Four-scatterer model. The homogeneous background has a velocity of 2.2 km/s and the source wavelet is a Ricker wavelet with a peak frequency of 15 Hz. The star shows the source location and the triangles show the receiver distribution and the dots mark the scatterers. b) the shot gather recorded by receivers along the top part of the model with the shot centred at $x = 2000$ m.

lations are created for sources along the bottom of the model in Fig. 6(a) and pressure seismograms are recorded along the top part. A shot gather with a 15 Hz Ricker wavelet is displayed in Fig. 6(b), which shows the strong direct arrivals and the weak scattered arrivals from the four scatterers in the model.

The $m(\mathbf{x}, t)$ image is calculated for the data in Fig. 6(b) and slices of the migration amplitudes at the trial excitation time of 0 s are displayed to give the sinc-like curves in Fig. 7. The time values t represent the time shifts in migration equation (4) and the image $m(\mathbf{x}, t)$ is computed using a two-way reverse-time migration method with the exact velocity and the scatterer model. The image for the original gather in Fig. 6(b) is denoted as $m^{dir}(\mathbf{x}, t)$, because the image amplitudes are dominated by those from the backpropagated direct waves. To study the image resolution of the scattered waves, a *scattered* shot gather where only scattered energy is present is obtained by muting the direct waves from the gather in Fig. 6(b). The slice of the migration amplitude at the time of 0 s for this *scattered* gather, $m^{scat}(\mathbf{x}, t)$, is shown in Fig. 7. Comparing these two slices indicates that the scattered waves provide a higher resolution than the original data and so provide a larger effective aperture for the source location. For the $m^{dir}(\mathbf{x}, t)$ case the direct waves are dominant and mask the imaging contribution from the scattered waves.

The effect of the receiver aperture on image resolution is now analysed for both the original and *scattered* shot gathers. By using only the central half of the traces in these two gathers, we recalculate the images, which are denoted by $m^{\frac{dir}{2}}(\mathbf{x}, t)$ and $m^{\frac{scat}{2}}(\mathbf{x}, t)$ and the slices at the time of 0 s are shown in Fig. 7. The comparison between slices calculated from full and half aperture data shows that when the recording aperture is halved, the image of the original data shows much lower

lateral resolution of the source location, while no apparent difference in lateral resolution is observed for the images associated with the scattered waves.

Figure 7 reveals the lateral resolution (i.e., width between adjacent zero crossings) for these four different situations. Also, the Rayleigh resolution limit (Schuster 2009) $\Delta x = \frac{z\lambda}{2L}$ is calculated for the full and half aperture data, where z, L and λ denote the depth of the source, half width of the recording aperture and the wavelength respectively. The comparison between lateral resolution measured from the migration images and the prediction from the Rayleigh resolution limits shows that the lateral resolution limit for the image computed from the original data largely follows the Rayleigh resolution limit but the scattered waves provide a much higher resolution even when the receiver aperture width is halved. For comparison, the lateral resolution obtained from the *scattered* wave shot gather with the half receiver-aperture of traces is about 67.7 m, i.e., less than 1/9 of the lateral resolution given by the original data and less than 1/6 of the prediction from the Rayleigh resolution limit ($\Delta x = \frac{z\lambda}{2L}$) of 391 m for the dominant wavelength of 146.7 m.

Validation of super-stacking

Numerical experiments are used to validate the super-stacking formula for signal enhancement:

$$SNR^{TRM} \propto \sqrt{MN} \propto \sqrt{(T_T/P)N}, \tag{5}$$

where T_T is the total time in a trace, SNR^{TRM} is the signal-to-noise ratio in the migration amplitude obtained with the time reversal mirror approach, P is the dominant period of the arrivals, M is the number of reflected, scattered or transmitted events in a trace and N is the number of traces. In
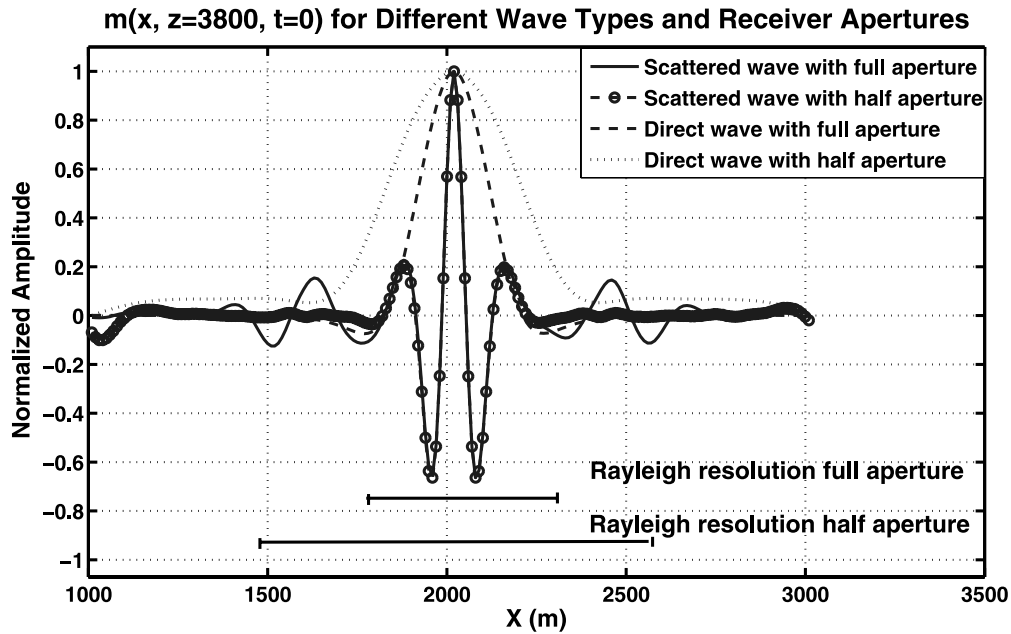
Figure 7 The migration curves $m^{dir}(\mathbf{x}, t)$, $m^{\frac{dir}{2}}(\mathbf{x}, t)$, $m^{scat}(\mathbf{x}, t)$ and $m^{\frac{scat}{2}}(\mathbf{x}, t)$. Migrating the direct waves leads to the typical Rayleigh-like resolution widths of the sinc-like function image, while the scattered data curves beat the Rayleigh-like horizontal resolution limit for the dominant frequency 15 Hz of the data by factors of 6 and 10 respectively. The main lobe widths of these four curves are in the ratio of 1:1:5.7:9.7.
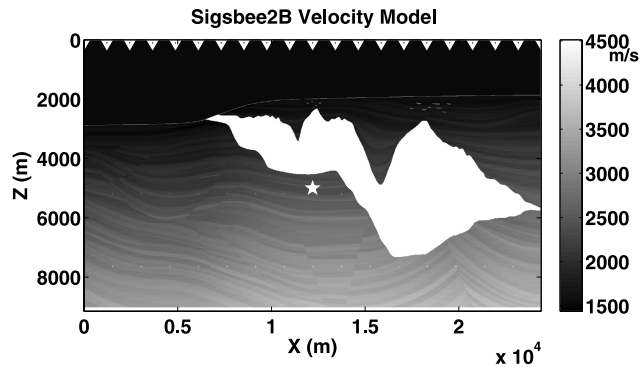

Figure 8 The Sigsbee 2B velocity model. The star shows the source location and the triangles represent the surface receivers.

equation (5) we approximate the number of events in a trace (M) by T_T/P. The detailed derivation of $SNR^{TRM} \propto \sqrt{MN}$ is given in Appendix A. The ratio T_T/P can be considered as a rough approximation to M, the number of distinguishable events in a trace. Here we assume that all the events have similar amplitudes. When geometrical spreading effects and transmission energy losses are significant, extra terms must be incorporated into the factor SNR^{TRM}.

A finite-difference solution to the 2D acoustic wave equation is used to generate shot gathers for the Sigsbee model in Fig. 8. The Sigsbee model is a complicated salt body that might represent structures seen in salt mines throughout the world, e.g., Remond mine, Utah, USA. The shots are buried at depths of about 5.0 km near the salt interface and receivers are along a horizontal line just below the free surface. One example of the shot gathers is shown in Fig. 9(a). Noise is added to the traces and they are migrated using equation (4) to get a noisy migration amplitude shown as the dashed curve in Fig. 9(b). The signal-to-noise ratio of the migration amplitude is computed by subtracting this migration amplitude from the noise-free image (solid curve in Fig. 9b) associated with the data without additive noise to get an image difference, and dividing the energy of the noise-free image by the energy of the image difference. This procedure is repeated except that a time window of duration T_T is applied to the shot gather so that only the first arrivals are used for migration. The signal-to-noise ratio of the new migration amplitude is computed. The window length T_T is gradually increased and the resulting migration amplitudes and their signal-to-noise ratios are computed. Figure 9(c) shows the resulting $log(T_T/P)$ versus $log(SNR)$ plot and numerically validates the trend predicted by equation (5). A constant is subtracted from the logarithmic curve for the SNR predicted with equation (A13) to fit it with the logarithmic curve of the numerical SNR; this is because the term $\frac{|(d_1(\mathbf{g}_1,t\,|\,\mathbf{s},0),g_1(\mathbf{g}_1,t\,|\,\mathbf{s},0))|}{|[(n_k(\mathbf{g}_i,t),g_k(\mathbf{g}_i,t\,|\,\mathbf{s},0))]|}$ in equation (A13) is not included in $log(T_T/P)$.
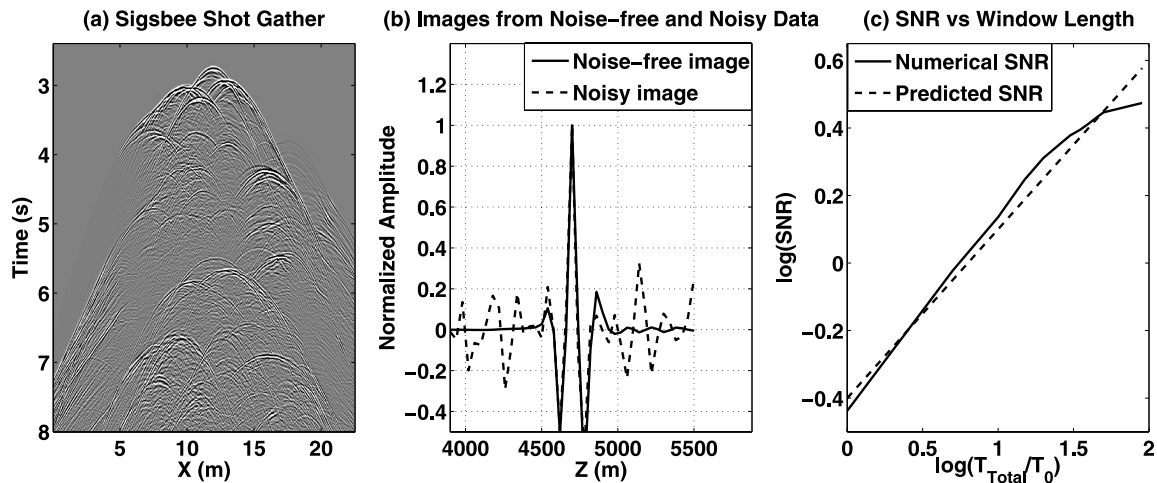
Figure 9 a) Shot gather generated from the Sigsbee model in Fig. 8. b) The migration amplitudes $m(\mathbf{x}, 0)$ for the noise-free data (solid curve) and noisy data (dashed curve). c) The SNR versus T_T/P logarithmic plot computed from the migration traces for different window lengths P. The dashed curve is predicted from equation (5).

FIELD SEISMIC EXPERIMENT

To validate the time reversed mirror scheme for locating trapped miners and its high-resolution and super-stacking properties, we carried out a seismic experiment along a cliff in Moab, Utah. Figure 10(a) shows a cross-section sketch of the experiment site and source-receiver geometry and Fig. 10(b) shows the actual cliff. The recording array is deployed on the top of the cliff at a height of about 60 m and the array is 45 m away from the edge of the cliff. This means the straight line distance between the sources and receivers is 75 m or greater. Figure 10(b) is a picture taken at the experiment site. The seismic source is a sledge hammer striking the rock at the bottom of the cliff.

The recording array consists of 72 receivers with a receiver interval of 2 metres; 21 shots with a shot spacing of 4 metres are excited to generate the seismic data to test the scheme of locating seismic sources with time reversal mirrors. Another 21 shots with a 1 m shooting spacing are excited to test the high-resolution property of time reversal mirrors. At each shot location, two different files are recorded: the first one is the SOS call, which is a shot gather with only one stack recorded at the receivers on the top and representing the vibrations from the miners $d(\mathbf{g}, t|\mathbf{s}, 0)$ in equation (4), also shown in Fig. 11(a); and the second file represents the natural Green's functions $g(\mathbf{g}, t|\mathbf{s}, 0)$ which are obtained by stacking traces generated by 10 stacks at the same location S. In the field data acquisition we excite multiple strikes of the hammer sources at the same location and stack the traces together to reduce noise and amplify the signal (Fig. 11b). In this test, the data are

acquired with a very high signal-to-noise ratio, and the traces from the SOS call and stacked Green's functions appear very similar. The frequency band of the field data is estimated to be from 8–204 Hz. The field gathers are preprocessed with a band pass filter (8–204 Hz) and amplitude normalization. Then the gathers are trace normalized to correct the differences in geophone coupling, where the amplitude values of each trace are divided by the maximum absolute amplitude of that trace.

In this field test, the P-wave velocity is estimated from the collected data to be 1364 m/s and the peak frequency of the data is 42 Hz (Fig. 12) to give a dominant wavelength of 16.2 m; thus, the Rayleigh resolution limit is computed to be $\frac{\lambda * Z}{2 * L} = \frac{16.2 * 75}{2 * 142} = 4.3$ m, where λ is the dominant wavelength $= \frac{V_p}{2 * Frequency}$, Z is the source-receiver offset, and L is the profile length.

Locating the trapped miners

The miner location scheme is tested with this Moab dataset. Applying the time reversal mirror approach to the SOS signal (i.e., $d(\mathbf{g}, t|\mathbf{s}, 0)$ in equation (2)) yields the migration amplitude $m(\mathbf{x}, 0)$ shown in Fig. 13(a,b) for two selected locations of the source. Repeating the process for all 21 SOS shot gathers gives the correct locations of the miners. These results are consistent with those for a time reversal mirror test in a copper mine in Arizona (Hanafy et al. 2009), and demonstrate that locating trapped miners using the time reversal mirror approach is successful for the shallow case study investigated here.
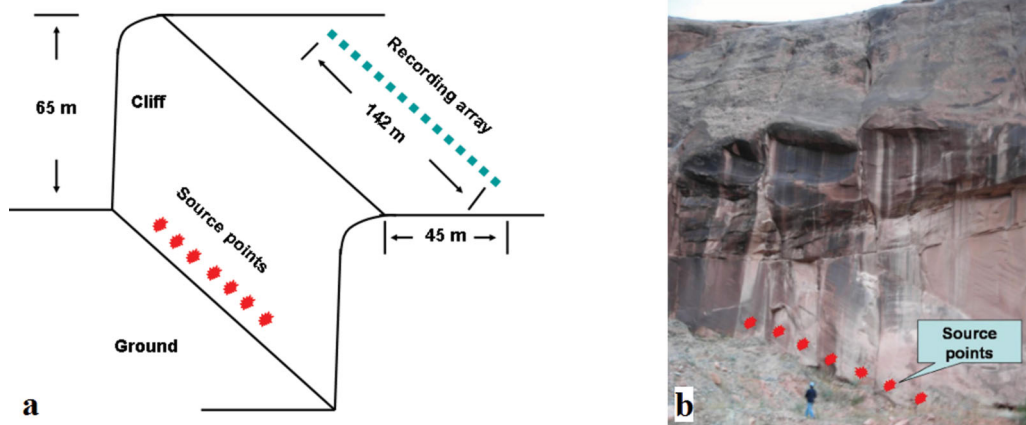
Figure 10 a) Sketch showing the source and receiver lines for the field test along a cliff in Moab, Utah. b) A photo taken at the experiment site in Moab, Utah. A hammer hitting at the source points shown in the figure is used to generate the seismic waves. The recording array is deployed on the top of the cliff, not visible in this photo.

Figure 11 SOS and Green's function examples for the Moab experiment. Here only the first 0.5 s of the 1 s records are displayed. a) A SOS shot gather. b) A natural Green's function. Each trace is normalized by its maximum amplitude value.
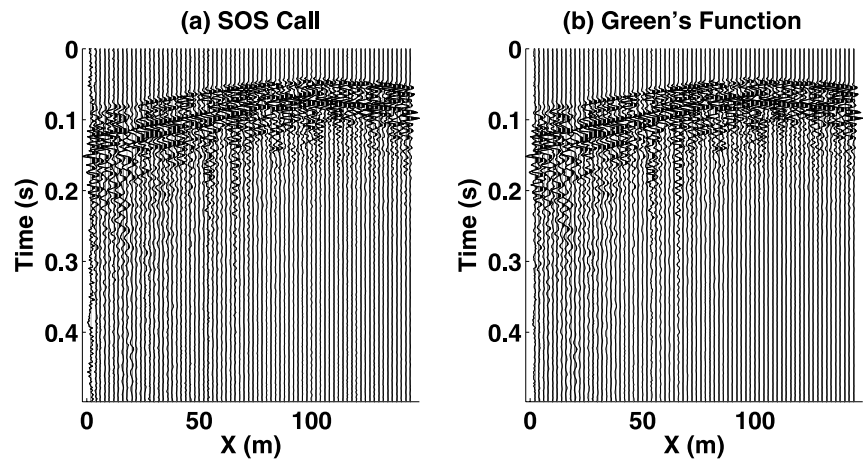
A more realistic scenario is that the source excitation time of the recorded SOS data source is unknown, so a time shift is applied to the recorded data. These shifted data are then migrated using equation (2), and the plot of $m(\mathbf{x}, t)$ in Fig. 14 shows the maximum value at the correct source location and excitation time.

Practical issues with locating miners using time reversal mirrors include the sensitivity of accurate imaging with respect to medium changes caused by the mine collapses, the signal strength in the real mining environment and the influence of weather conditions on the permanent geophone arrays. The synthetic tests in Appendix B show correct source identification when the rock properties are perturbed over an area of $16\lambda^2$, where λ denotes the dominant wavelength. Other issues involved with mining environments, the real noise in mines for example, need further investigation.

Demonstration of the high-resolution property

The high-resolution property of the time reversal mirror approach is also tested on the Moab data. Similar to the validation of high-resolution with the synthetic data, the scattered energy in the field data traces is separated from the direct arrivals. We apply a time window that includes the first 0.125 second record after the first break of each trace and separate the gather into two parts: the early arrivals inside the time window and the late arrivals after the time window. We take the early arrivals as the direct-wave shot gather where the direct waves are dominant and define the late arrivals as the scattered shot gather where mainly scattered energy is present. Figure 15(b) shows an example of the scattered shot gather. Then migration amplitudes are computed from both data sets for the full 72-trace aperture and 36-trace half receiver
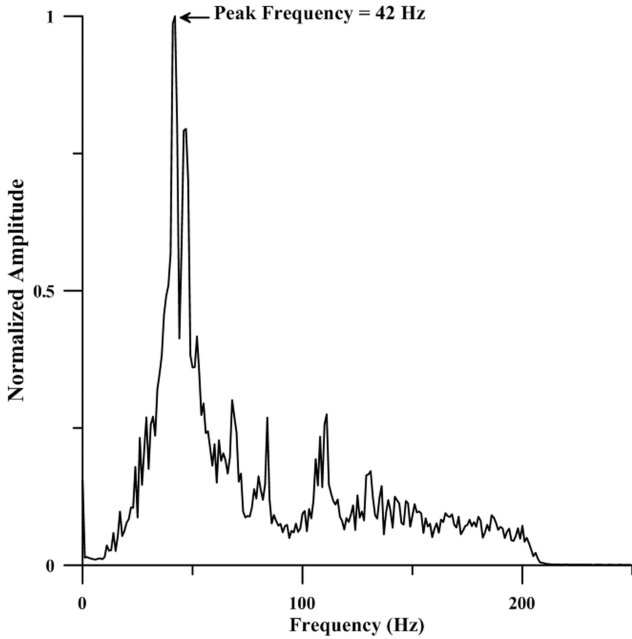
Figure 12 Average amplitude spectrum of one shot gather, the power spectrum of each trace is calculated, then all amplitude spectrums are summed and normalized. The frequency in these data is 42 Hz.
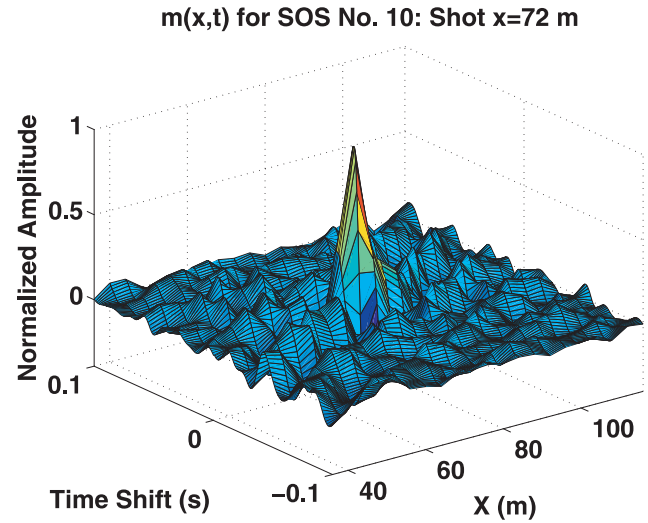

Figure 14 The migration amplitude with trial time shifts $m(\mathbf{x}, t)$ computed from the same SOS shot gather as Fig. 13(a). The peak in the image shows the actual SOS location and the excitation time.

apertures. Figure 16 shows the four migration amplitudes: $m^{dir}(\mathbf{x}, 0)$ calculated from only direct waves using the full aperture width, $m^{\frac{dir}{2}}(\mathbf{x}, 0)$ computed from only direct waves using a half aperture width, $m^{scatt}(\mathbf{x}, 0)$ obtained from only scattered data using the full aperture width and $m^{\frac{scatt}{2}}(\mathbf{x}, 0)$ from only scattered data using a half aperture width. Note that we first recorded the Green's function then recorded the

SOS gather that is not stacked into the previously recorded Green's function gather. This ensures that the random noise in the SOS gather is not stacked into the Green's function gather.

If the horizontal spatial resolution limit is defined as the width at half the maximum amplitude, see arrows in Fig. 16, then the resulting images show that 1) the horizontal spatial resolution limits of $m^{scatt}(\mathbf{x}, 0) = 1.5$ m and $m^{\frac{scatt}{2}}(\mathbf{x}, 0) = 1.5$ m are much higher than that of $m^{dir}(\mathbf{x}, 0) = 5.3$ m and $m^{\frac{dir}{2}}(\mathbf{x}, 0) = 6.6$ m and 2) if only direct arrivals are used, the horizontal resolution decreases as the receiver aperture
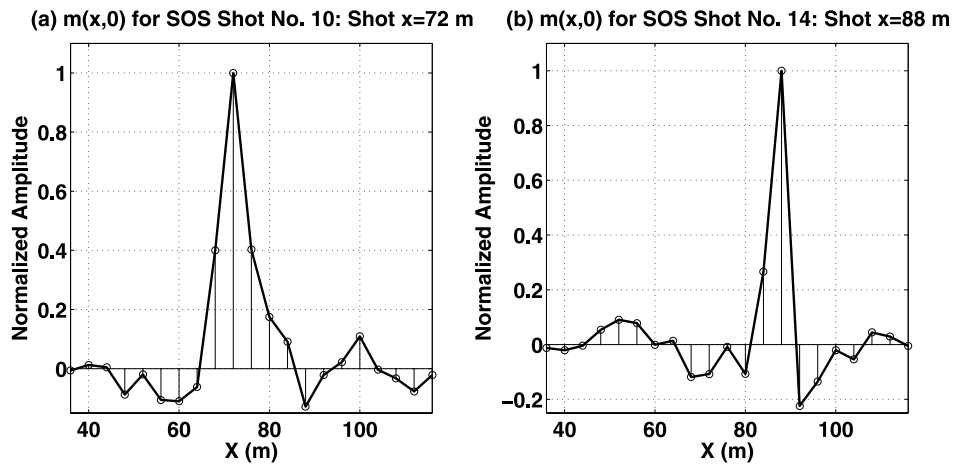

Figure 13 Two examples showing the results of the time reversal mirror approach in locating trapped miners. a) $m(\mathbf{x}, 0)$ for the SOS call from X = 72 m. b) $m(\mathbf{x}, 0)$ for the SOS call from X = 88 m. In both cases the peak value shows the actual SOS shot location.
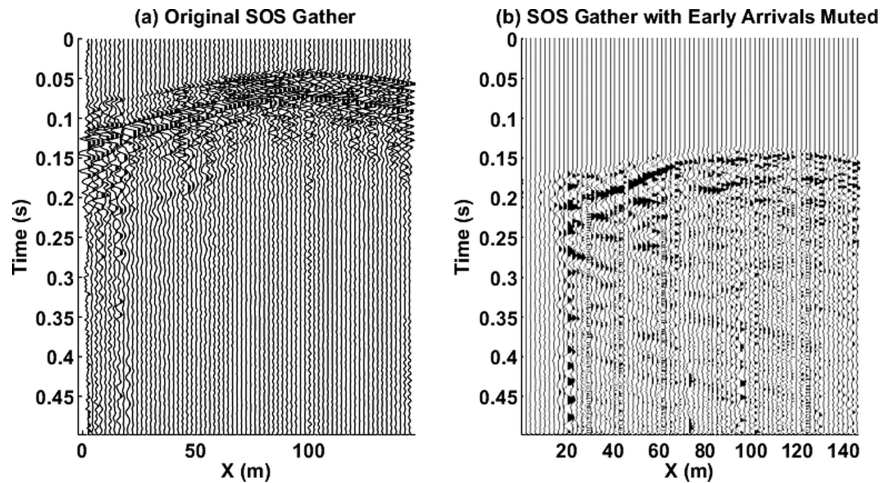
Figure 15 The a) original and b) scattered SOS gather. (b) is obtained by muting the first 0.125 s record after the first break of the each trace from (a) and then apply a 50-samples taper afterward.
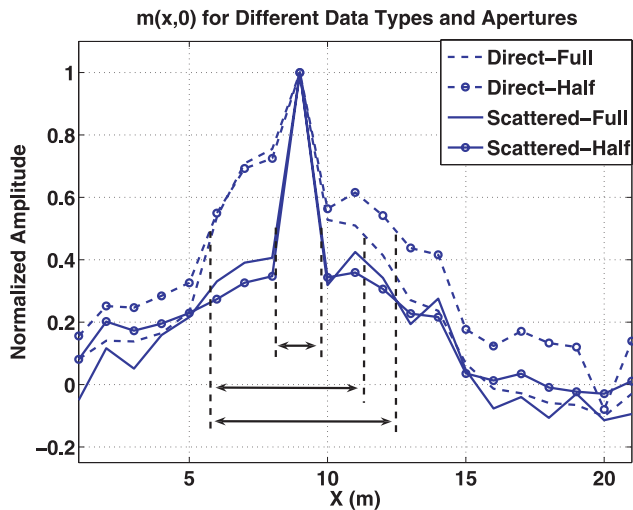

Figure 16 Demonstration of high-resolution with the data acquired from Moab, Utah. Amplitude curves are displayed for the direct-wave shot gather with full aperture, direct-wave shot gather with half aperture, scattered-wave shot gather with full aperture and scattered-wave shot gather with half aperture.

decreases. In comparison the resolution limit from the scattered data is the same when the aperture is halved. Our results using only scattered waves show a spatial resolution that is 3.5–4.5 times better than the Rayleigh resolution. This suggests that there are strong scatterer points between the source and receiver lines. This is a conjecture because we do not know if the interior of the sandstone contains significant scatterers, however, there is a cave within one to two wavelengths

distance from the source points; the entrance of this cave is man-made and is approximately 4 m in diameter.

The resolution comparisons, not shown, for the other migration amplitudes computed for data from 16 of the 21 shot points show the same trend. The test results for this field data are consistent with the synthetic data results and again validate the high-resolution property of time reversed mirrors. However, this enhanced resolution does not approach the order of magnitude improvement seen in electromagnetic experiments (Lerosey *et al.* 2007).

Demonstration of the super-stacking property

In an actual mine accident, the SOS call $d(\mathbf{g}, t|\mathbf{x}, 0)$ from the trapped miners is usually contaminated with strong noise. To show the time reversal mirror resilience to additive noise, band-pass filtered random noise is added to the SOS call collected in the experiment (Fig. 17), and equation (4) is implemented with the noisy SOS call. The results in Fig. 18(a,b) show that the location of the trapped miners is identified even with the SOS call having a signal-to-noise ratio of 1/1226. If the noise is coherent then such noise should be deterministically removed prior to correlation.

DISCUSSION

In the trapped miners' application, realistic noise in mines is more complex than white noise, and further analysis of real background noise and the removal of coherent noise
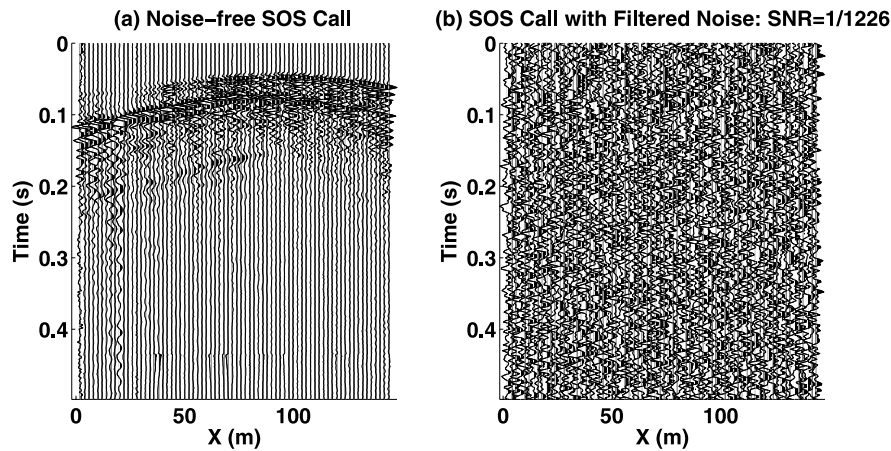
Figure 17 a) Noise-free SOS gather. b) The SOS gather with additive noise. Filtered random noise is added to the SOS gather and the signal-to-noise ratio is 1/1226. No events can be identified in this noisy gather.
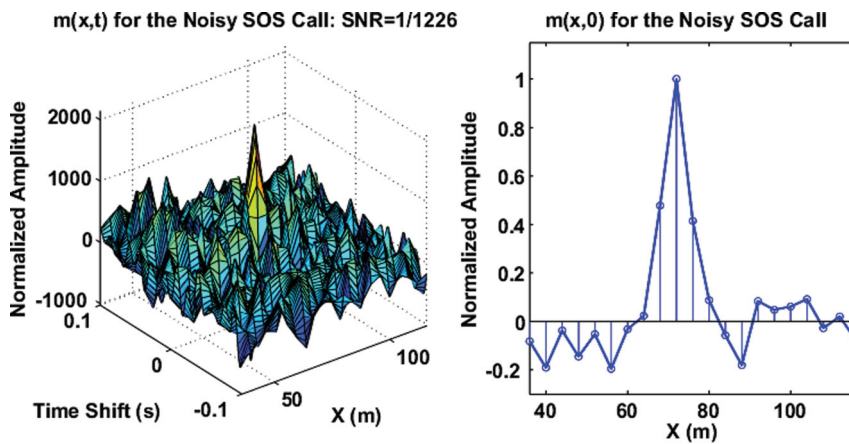

Figure 18 a) The migration image $m(\mathbf{x}, t)$ with trial time shift computed for the noisy SOS gather shown in Fig. 17(b). b) The zero time shift section $m(\mathbf{x}, 0)$ from the migration amplitude shown in (a).

are needed for the practical application of this technique. To apply the time reversal mirrors method to other areas in exploration geophysics, the natural Green's function is needed, which could be a limiting factor in some applications. For example in hydraulic fracturing operations, this Green's function can be recorded either by vertical seismic profiling experiments, seismic during the drilling processing, or by perforation shots that shoot along the drill string. These Green's functions can then be extrapolated using the local velocity around the well (Cao *et al.* 2008) and then used to locate the sources of the localized events due to hydraulic fracturing.

Scattered waves have the potential of providing spatial resolution beyond the Rayleigh limits because they increase the apparent aperture of the recording line. In some of our tests, the scattered waves were separated from the strong direct ar-

rivals before applying time reversal mirror imaging. For some of the field data tests, we set a time window with a specific length after the picked first break and muted the traces inside the window to make the scattered energy dominant. This technology can also be used to help locate sources associated with enhanced oil recovery operations (Cao *et al.*, 2008). The recorded Green's function is affected by the density variations and the size of scatterers in the medium (Vlastos *et al.*, 2003 and 2007).

Recent results by Lerosey *et al.* (2007) showed that time reversed mirrors can be used for focusing electromagnetic data to its origin with a resolution of less than $\frac{\lambda}{30}$. This enhanced resolution goes beyond the Abbe limit and is attributed to that provided by evanescent waves converted into propagation waves near the source location. Their results suggest that, ideally, reverse time migration, if the exact velocity model is

known, might also achieve such a high resolution; but practically achieving this high resolution for seismic imaging will likely be an elusive goal for some time.

CONCLUSIONS

A time-reversal mirror imaging scheme is presented for locating buried seismic sources. Tests with both synthetic and field data clearly suggest that time reversal mirrors can reliably locate trapped miners, though practical issues related to the actual mining environment need further study. Results with both synthetic and field data also demonstrated the high-resolution and super-stacking properties of this scheme. High-resolution is achieved by backpropagating the scattered waves after separating them from the direct arrival data. Synthetic tests show that the horizontal resolution limit associated with the scattered waves can be 9 times less than the Rayleigh resolution limit and the field data results from the Moab experiment show that the resolution limit from scattered waves is 3.5–4.5 times better than that from the direct waves. A crucial step in achieving the high-resolution benefit is to properly separate the scattered energy from the strong direct arrivals. Otherwise, the high resolution components from the scattered waves can be easily masked by the strong direct arrivals in the imaging procedure.

The super-stacking property of time reversal mirrors is also demonstrated by showing that time reversal mirror enhance the signal by a factor proportional to $\sqrt{N\frac{T_T}{P}}$ and significantly exceeds the $\sqrt{N}$ enhancement predicted by stacking alone. Here N is the number of receivers, P is the dominant period of the source wavelet, T is the recording-time range with visible events and the scattered events are assumed to have the same amplitude as the direct arrivals. Both synthetic and field data tests show the strong noise resilience of time reversal mirrors by providing reliable images in the presence of strong random noise.

Both high-resolution and super-stacking results are achieved with the existence of scattering points. To our knowledge, this is one of the first experimental verifications of the high-resolution property with a realistic seismic experiment. We also believe that this is the first demonstration of the super-stacking property with field data.

The results in our paper may have important implications in subsalt imaging because the time reversal mirrors operation is equivalent to reverse time migration that uses an exact velocity model. This suggests that a more accurate estimate of $v(x, y, z)$ will lead to better resolution and signal-to-noise ratios in the reverse time migration images. Moreover, the time reversal mirror method might be used to locate hydro-frac sources in an EOR experiment.

LIST OF SYMBOLS AND ABBREVIATIONS

Symbol	Description
c	Velocity
$d(\mathbf{g}, t\|\mathbf{s}, 0)$	Seismic data recorded at receiver $\mathbf{g}$ with source $\mathbf{s}$ excited at time 0
$d_k(\mathbf{g}_i, t\|\mathbf{s}, 0)$	The kth event of the ith trace
$E[]$	The statistic expectation
$g(\mathbf{g}, t\|\mathbf{x}, 0)$	Green's function for a source at $\mathbf{x}$ excited at time 0
L	Half width of the recording aperture
$m(\mathbf{x}, t)$	Migration image
$m^{dir}(\mathbf{x}, t)$	Migration image calculated from only direct waves using the full aperture width
$m^{\frac{dir}{2}}(\mathbf{x}, t)$	Migration image calculated from only direct waves using the half aperture width
$m^{scatt}(\mathbf{x}, 0)$	Migration image obtained from only scattered data using the full aperture width
$m^{\frac{scatt}{2}}(\mathbf{x}, 0)$	Migration image obtained from only scattered data using a half aperture width
M	Number of events in the records
N	Number of traces
$n_k(\mathbf{g}_i, t)$	The kth segment of the ith noise trace with the same time range as that of the kth event in $d(\mathbf{g}_i, t\|\mathbf{s}, 0)$
P	Dominant period
T_T	The total time in a trace
$w(t)$	Band limited source wavelet
z	The depth of the source point
λ	The wavelength
τ_{xg}	Travel time between source x and receiver g

REFERENCES

Cao W., Fei T.W., Luo Y., Alfaraj M.N., Schuster G.T. and Boonyasiriwat C. 2008. Estimation of hydrofracture source location with time reversal mirrors. 78th SEG meeting, Las Vegas, Nevada, USA, Expanded Abstracts, 1421–1424.

Derode A., Roux P. and Fink M. 1995. Robust acoustic time reversal with high-order multiple scattering. *Physics Review Letters* **75**, 4206–4209.

Fink M. 1993. Time-reversal mirrors. *Journal of Physics D, Applied Physics* **26**, 1333–1350.

Fink M. 1997. Time-reversal acoustics. *Physics Today* **50**, 34–40.

Fink M. 2006. Time-reversal acoustics in complex environments. *Geophysics* **71**, SI151–SI164.

Fink M. 2008. Time reversal waves and super resolution. *Journal of Physics* **124**. doi:10.1088/1742-6596/124/012004

Gajewski D. and Tessmer E. 2005. Reverse modeling for seismic event characterization. *Geophysical Journal International* **163**, 276–284.

Hanafy S.M., Cao W., McCarter K. and Schuster G.T. 2009. Using super-stacking and super-resolution properties of time-reversal mirrors to locate trapped miners. *The Leading Edge* **28**, 302–307.

Lerosey G., de Rosny J., Tourin A. and Fink M. 2007. Focusing beyond the diffraction limit with far-field time reversal. *Science* **315**, 1120–1122.

McMechan G.A. 1982. Determination of source parameters by wavefield extrapolation. *Geophysical Journal of the Royal Astronomical Society* **71**, 613–628.

McMechan G.A., Luetgert J.H. and Mooney W. 1983. Imaging of earthquake sources in Long Valley Caldera, California. *Bulletin of the Seismological Society of America* **75**, 1005–1020.

Nemeth T., Wu C. and Schuster G.T. 1999. Least-squares migration of incomplete reflection data. *Geophysics* **64**, 208–221.

Roux P. and Fink M. 2000. Time reversal in a waveguide: Study of the temporal and spatial focusing. *Journal of the Acoustical Society of America* **107**, 2418–2429.

Scales J.A. and Snieder R. 1997. Humility and nonlinearity. *Geophysics* **62**, 1355–1358.

Schuster G.T. 2002. Reverse-time migration = Generalized diffraction stack migration. 72nd SEG meeting, Salt Lake City, Utah, USA, Expanded Abstracts, 1280–1283.

Schuster G.T. 2009. *Seismic Interferometry*. Cambridge University Press.

Snieder R. and Scales J.A. 1998. Time-reversed imaging as a diagnostic of wave and particle chaos. *Physics Review E* **58**, 5668–5675.

Thurber C. and Rabinowitz N. 2000. *Advances in Seismic Event Location*. Kluwer Academic Publishers.

Vigoureux J.M., Depasse F. and Girard C. 1992. Superresolution of near-field optical microscopy defined from properties of confined electromagnetic waves. *Applied Optics* **31**, 3036-3045, doi:10.1364/AO.31.003036

Vlastos S., Liu E., Main I.G. and Li X.Y. 2003. Numerical simulation of wave propagation in media with discrete distributions of fractures: effects of fracture sizes and spatial distributions. *Geophysical Journal International* **152**, 649–668.

Vlastos S., Liu E., Main I.G. and Narteau C. 2007. Numerical simulation of wave propagation in fractured media: scattering attenuation at different stages of the growth of a fracture population. *Geophysical Journal International* **171**, 865–880.

Waldhauser F. and Ellsworth W. 2000. A double-difference earthquake location algorithm: method and application to the northern Hayward fault, California. *Bulletin of the Seismological Society of America* **90**, 1353–1368.

Zhang X. and Liu Z. 2008. Superlenses to overcome the diffraction limit. *Nature Materials* **7**, 435–441.

APPENDIX A: DERIVATION OF THE SUPER-STACKING FORMULA

Equation (4) represents the time reversal mirror approach for locating seismic sources with a trial time shift. Suppose we know the actual source excitation time and set it as 0, the image of the source location is formulated as:

$$m(\mathbf{x}, 0) = \sum_g [d(\mathbf{g}, t|\mathbf{s}, 0) \otimes g(\mathbf{g}, t|\mathbf{x}, 0)]\,|_{t=0}$$
$$= \sum_g \langle d(\mathbf{g}, t|\mathbf{s}, 0), g(\mathbf{g}, t|\mathbf{x}, 0)\rangle, \qquad (A1)$$

where $<,>$ denotes the temporal dot product operation between vectors.

When we assume that the noise-free data $d(\mathbf{g}, t|\mathbf{s}, 0)$ have N traces with M distinct events of similar amplitudes in each trace (i.e., geometrical spreading and attenuation effects are negligible), the ith trace of the data $d(\mathbf{g}, t|\mathbf{s}, 0)$ can be represented as:

$$d(\mathbf{g}_i, t|\mathbf{s}, 0) = \sum_{k=1}^{M} d_k(\mathbf{g}_i, t|\mathbf{s}, 0), \qquad (A2)$$

where $d_k(\mathbf{g}_i, t|\mathbf{s}, 0)$ denotes the kth event of the ith trace. Similarly, the pre-recorded Green's functions can be formulated as $g(\mathbf{g}_i, t|\mathbf{x}, 0) = \sum_{k=1}^{M} g_k(\mathbf{g}_i, t|\mathbf{x}, 0)$; a white noise dataset is written as $n(\mathbf{g}_i, t) = \sum_{k=1}^{M} n_k(\mathbf{g}_i, t)$, where $n_k(\mathbf{g}_i, t)$ denotes the kth segment of the ith noise trace with the same time range as that of the kth event in $d(\mathbf{g}_i, t|\mathbf{s}, 0)$; and the data with white noise can be given as $d^{noisy}(\mathbf{g}_i, t|\mathbf{s}, 0) = \sum_{k=1}^{M} (d_k(\mathbf{g}_i, t|\mathbf{s}, 0) + n_k(\mathbf{g}_i, t))$.

For the conventional migration scheme to locate seismic sources, only the first arrival event is included in the migration imaging process and identifying the source location from the data with white noise can be described as

$$m^{conv.}(\mathbf{x}, t = 0)$$
$$= \sum_{i=1}^{N} \langle d_1(\mathbf{g}_i, t|\mathbf{s}, 0) + n_1(\mathbf{g}_i, t), g_1(\mathbf{g}_i, t|\mathbf{x}, 0)\rangle$$
$$= \sum_{i=1}^{N} \langle d_1(\mathbf{g}_i, t|\mathbf{s}, 0), g_1(\mathbf{g}_i, t|\mathbf{x}, 0)\rangle$$
$$+ \sum_{i=1}^{N} \langle n_1(\mathbf{g}_i, t), g_1(\mathbf{g}_i, t|\mathbf{x}, 0)\rangle. \qquad (A3)$$

Then the signal-to-noise ratio of the migration amplitude in equation (A3) gives

$$SNR^{conv.} = \sqrt{\frac{\left(\sum_{i=1}^{N} \langle d_1(\mathbf{g}_i, t|\mathbf{s}, 0), g_1(\mathbf{g}_i, t|\mathbf{x}, 0)\rangle\right)^2}{\left(\sum_{i=1}^{N} \langle n_1(\mathbf{g}_i, t), g_1(\mathbf{g}_i, t|\mathbf{x}, 0)\rangle\right)^2}}. \quad (A4)$$

The first arrival events in all traces $d_1(\mathbf{g}_i, t|\mathbf{s}, 0)$ and Green's functions $g_k(\mathbf{g}_i, t|\mathbf{x}, 0)$ have similar amplitudes, we have

$$\left(\sum_{i=1}^{N} \langle d_1(\mathbf{g}_i, t|\mathbf{s}, 0), g_1(\mathbf{g}_i, t|\mathbf{x}, 0)\rangle\right)^2$$
$$\approx N^2 \langle d_1(\mathbf{g}_1, t|, 0), g_1(\mathbf{g}_1, t|\mathbf{x}, 0)\rangle^2. \quad (A5)$$

Here $\langle n_1(\mathbf{g}_i, t), g_1(\mathbf{g}_i, t|\mathbf{s}, 0)\rangle, i = 1, 2, \ldots, N$ can be viewed as an uncorrelated random series since $n_i(\mathbf{g}_i, t), i = 1, 2, \ldots, N$ are uncorrelated random noise and we have

$$\left(\sum_{i=1}^{N} \langle n_1(\mathbf{g}_i, t), g_1(\mathbf{g}_i, t|\mathbf{x}, 0)\rangle\right)^2$$
$$\approx N \cdot E[\langle n_1(\mathbf{g}_i, t), g_1(\mathbf{g}_i, t|\mathbf{x}, 0)\rangle]^2, \quad (A6)$$

where $E[]$ denotes the expectation operator. Substituting equations (A5) and (A6) into equation (A4) gives:

$$SNR^{conv.} \approx \sqrt{\frac{N^2 \langle d_1(\mathbf{g}_1, t|\mathbf{s}, 0), g_1(\mathbf{g}_1, t|\mathbf{x}, 0)\rangle^2}{N \cdot E[\langle n_1(\mathbf{g}_i, t), g_1(\mathbf{g}_i, t|\mathbf{x}, 0)\rangle]^2}}$$
$$= \sqrt{N} \frac{|\langle d_1(\mathbf{g}_1, t|\mathbf{s}, 0), g_1(\mathbf{g}_1, t|\mathbf{x}, 0)\rangle|}{|E[\langle n_1(\mathbf{g}_i, t), g_1(\mathbf{g}_i, t|\mathbf{x}, 0)\rangle]|}. \quad (A7)$$

Equation (A7) shows that stacking along the first arrival event enhances the signal-to-noise ratio of the image by the factor of $\sqrt{N}$.

When we migrate the noisy data $d^{noisy}(\mathbf{g}_i, t|\mathbf{s}, 0)$ with the time reversal mirror scheme in equation (A1), where all the M events in the data are included in the imaging process, the image is represented as

$$m^{TRM}(\mathbf{x}, t = 0)$$
$$= \sum_{i=1}^{N} \left\langle \sum_{k=1}^{M} (d_k(\mathbf{g}_i, t|\mathbf{s}, 0) + n_k(\mathbf{g}_i, t)), \sum_{k=1}^{M} g_k(\mathbf{g}_i, t|\mathbf{x}, 0) \right\rangle. \quad (A8)$$

Since there is no overlap between different events and assuming that the time shift caused by the deviation of $\mathbf{x}$ from $\mathbf{s}$ is negligible, we have $\langle d_m(\mathbf{g}_i, t|\mathbf{s}, 0) + n_m(\mathbf{g}_i, t), g_n(\mathbf{g}_i, t|\mathbf{s}, 0)\rangle = 0$

if $m \neq n$, so that equation (A8) can be written as

$$m^{TRM}(\mathbf{x}, t = 0)$$
$$= \sum_{k=1}^{M} \sum_{i=1}^{N} \langle d_k(\mathbf{g}_i, t|\mathbf{s}, 0) + n_k(\mathbf{g}_i, t), g_k(\mathbf{g}_i, t|\mathbf{x}, 0)\rangle$$
$$= \sum_{k=1}^{M} \sum_{i=1}^{N} \langle d_1(\mathbf{g}_i, t|\mathbf{s}, 0), g_1(\mathbf{g}_i, t|\mathbf{x}, 0)\rangle$$
$$+ \sum_{k=1}^{M} \sum_{i=1}^{N} \langle n_1(\mathbf{g}_i, t), g_1(\mathbf{g}_i, t|\mathbf{x}, 0)\rangle, \quad (A9)$$

and the signal-to-noise ratio in the image is formulated as

$$SNR^{TRM} = \sqrt{\frac{\left(\sum_{k=1}^{M} \sum_{i=1}^{N} \langle d_k(\mathbf{g}_i, t|\mathbf{s}, 0), g_k(\mathbf{g}_i, t|\mathbf{x}, 0)\rangle\right)^2}{\left(\sum_{k=1}^{M} \sum_{i=1}^{N} \langle n_k(\mathbf{g}_i, t), g_k(\mathbf{g}_i, t|\mathbf{x}, 0)\rangle\right)^2}}. \quad (A10)$$

Applying the same assumptions for equations (A5) and (A6), we have

$$\left(\sum_{k=1}^{M} \sum_{i=1}^{N} \langle d_k(\mathbf{g}_i, t|\mathbf{s}, 0), g_k(\mathbf{g}_i, t|\mathbf{x}, 0)\rangle\right)^2$$
$$\approx M^2 N^2 \langle d_1(\mathbf{g}_1, t|\mathbf{s}, 0), g_1(\mathbf{g}_1, t|\mathbf{x}, 0)\rangle^2, \quad (A11)$$

and

$$\left(\sum_{k=1}^{M} \sum_{i=1}^{N} \langle n_k(\mathbf{g}_i, t), g_k(\mathbf{g}_i, t|\mathbf{x}, 0)\rangle\right)^2$$
$$\approx MN \cdot E[\langle n_1(\mathbf{g}_i, t), g_1(\mathbf{g}_i, t|\mathbf{x}, 0)\rangle]^2. \quad (A12)$$

Substituting equations (A11) and (A12) into equation (A10) gives

$$SNR^{TRM} \approx \sqrt{\frac{M^2 N^2 \langle d_1(\mathbf{g}_1, t|\mathbf{s}, 0), g_1(\mathbf{g}_1, t|\mathbf{x}, 0)\rangle^2}{MN[\langle n_1(\mathbf{g}_i, t), g_1(\mathbf{g}_i, t|\mathbf{x}, 0)\rangle]^2}}$$
$$= \sqrt{MN} \frac{|\langle d_1(\mathbf{g}_1, t|\mathbf{s}, 0), g_1(\mathbf{g}_1, t|\mathbf{x}, 0)\rangle|}{|E[\langle n_1(\mathbf{g}_i, t), g_1(\mathbf{g}_i, t|\mathbf{x}, 0)\rangle]|}, \quad (A13)$$

which shows for the time reversed mirror imaging approach that the signal-to-noise ratio in the image of the source location is enhanced by a factor proportional to $\sqrt{MN}$.

APPENDIX B: MINER LOCATION: TESTS ON THE EFFECT OF MEDIUM CHANGES CAUSED BY A MINE COLLAPSE

A potential problem with the time reversal mirror scheme for locating trapped miners is its sensitivity of time reversed
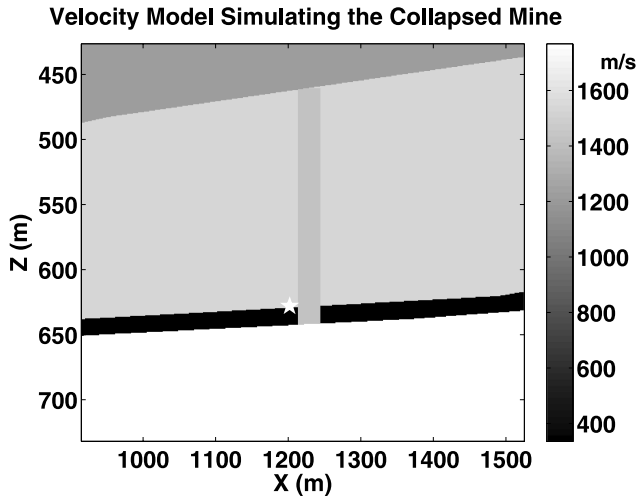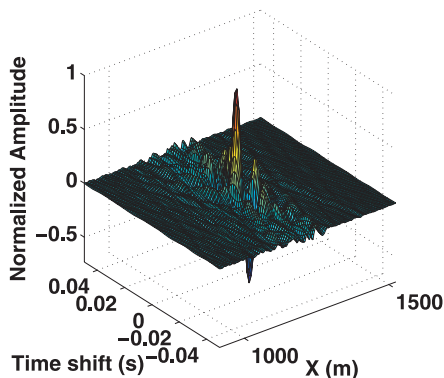
Velocity Model Simulating the Collapsed Mine

Figure B1 The partial velocity model containing a collapsed zone in the mine. The vertical grey block in the figure indicates the collapsed zone with a velocity of 1411 m/s and the black stripe denotes the mining tunnel. The velocity of the layer surrounding the collapsed zone is 1524 m/s. The trapped miner (star) strikes on the mining tunnel 11 m away from the collapsed zone.

mirror with respect to the medium changes caused by the mine collapse. To study the effect of medium changes on the location results, synthetic tests are conducted on the mine model shown in Fig. 2 and used the following procedures.

1 Simulate the collapsed mine by defining a collapsed zone near the mining tunnel with a lower velocity than that of the background layer;

2 Model the SOS call by calculating FD solutions to the acoustic wave equation for the collapsed mine model;

3 Image the location of the trapped miner using the SOS call generated in step 2 and the natural Green's functions recorded before the mine collapses.

Image of the Miner Location: Source x=1202 m

Figure B3 The time reversed migration location result for the SOS call simulated with the 183 m collapsed mine model. The dashed curve shows the result for the SOS call and Green's functions both generated with the model for the mine before collapse (Fig. 2) and the vertical dashed line shows the actual location of the miner.

Figure B1 shows part of the velocity model containing a collapse zone of 30 m width and 180 m height, indicated as the vertical block in the figure. The velocities of the collapsed zone and its surrounding layer are 1411 m/s and 1524 m/s respectively. The synthetic SOS call is generated for the model in Fig. B1 with the miner at 11 m away from the collapsed zone. The time reversal mirror scheme is implemented as step 3 describes and the results in Fig. B2 indicate that the image still gives an accurate location of the trapped miner though the image is distorted.

Then we enlarge the size of the collapsed zone in the mine model to be 183 m wide and 183 m high. Similar to the previous test, a synthetic SOS call is generated and the location of the trapped miner is obtained using the natural Green's

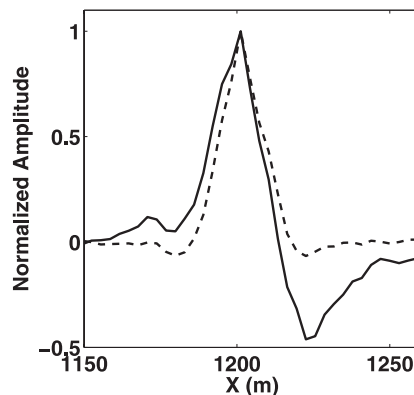**(a) Location Result with Time Shifts**   **(b) Location Result: 0 Time Shift**

Figure B2 The time reversed mirror location result for the SOS call generated with the mine model in Fig. B1. a) The location result with a trial time shift. The peak amplitude indicates a 0 time shift and a correct source location $x = 1202$ m. b) The section for 0 time shift from (a). The dashed curve shows the result for the SOS call and Green's functions, both generated with the model before the mine collapses (Fig. 2).
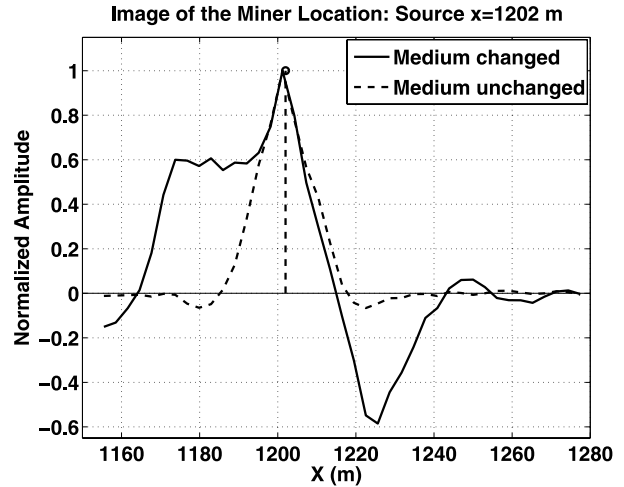
function recorded before the mine collapses. Figure B3 shows that the image still identifies out the correct source location though there is more ambiguity for the miner's location and the image is more distorted than shown in Fig. B2.

Tests on this mine model show, as the collapsed zone expands, that the resulting location image is more distorted and more ambiguity appears in the result. This issue needs further investigation for the practical application of the miner location scheme.